

Improved Cycling Performance of Li-Excess Cation-Disordered Cathode Materials upon Fluorine Substitution

Zhengyan Lun, Bin Ouyang, Daniil A. Kitchaev, Raphaële J. Clément, Joseph K. Papp, Mahalingam Balasubramanian, Yaosen Tian, Teng Lei, Tan Shi, Bryan D. McCloskey, Jinhyuk Lee,* and Gerbrand Ceder*

The recent discovery of Li-excess cation-disordered rock salt cathodes has greatly enlarged the design space of Li-ion cathode materials. Evidence of facile lattice fluorine substitution for oxygen has further provided an important strategy to enhance the cycling performance of this class of materials. Here, a group of $\text{Mn}^{3+}\text{-Nb}^{5+}$ -based cation-disordered oxyfluorides, $\text{Li}_{1.2}\text{Mn}^{3+}_{0.6+0.5x}\text{Nb}^{5+}_{0.2-0.5x}\text{O}_{2-x}\text{F}_x$ ($x = 0, 0.05, 0.1, 0.15, 0.2$) is investigated and it is found that fluorination improves capacity retention in a very significant way. Combining spectroscopic methods and ab initio calculations, it is demonstrated that the increased transition-metal redox ($\text{Mn}^{3+}/\text{Mn}^{4+}$) capacity that can be accommodated upon fluorination reduces reliance on oxygen redox and leads to less oxygen loss, as evidenced by differential electrochemical mass spectroscopy measurements. Furthermore, it is found that fluorine substitution also decreases the Mn^{3+} -induced Jahn–Teller distortion, leading to an orbital rearrangement that further increases the contribution of Mn-redox capacity to the overall capacity.

research on lithium-ion battery cathodes has been largely dominated by layered rock salt materials in the $\text{Li}_x(\text{Ni-Mn-Co-Al})_{2-x}\text{O}_2$ (NMCA) compositional space,^[3,4] in which redox activity is limited to Co and Ni. Cobalt in particular is expensive and relatively scarce compared to other 3d transition metals, such as Fe or Mn.^[1,3,5] The fact that the cathode structure has to be layered and remain layered upon cycling greatly restricts the changes which can be made to NMCA-type rock salt chemistries.

Recent progress in the development of Li percolation theory for rock salt compounds, in which Li transport still takes place even when the cations are disordered, has greatly enlarged the design space for cathode materials.^[6,7] Lifting the requirement that cations form an ordered (layered) structure enables the

use of various transition metal (TM) redox centers, including $\text{Mn}^{3+}/\text{Mn}^{4+}$,^[8,9] $\text{Mn}^{2+}/\text{Mn}^{4+}$,^[5,10] $\text{Cr}^{3+}/\text{Cr}^{5+}$,^[6,11] $\text{Mo}^{3+}/\text{Mo}^{6+}$,^[12] and $\text{V}^{3+}/\text{V}^{5+}$.^[11,13] Because these compounds need Li excess to achieve Li percolation,^[6,7] they typically also contain high valent charge compensators, such as Nb^{5+} ,^[8,9] Sb^{5+} ,^[14] Mo^{6+} ,^[15,16] and Ti^{4+} .^[16–18] In addition, fluorine substitution is facile in

1. Introduction

With the ever increasing demand for electrochemical energy storage, there is an urgent need for the development of cathode materials for lithium-ion batteries with higher energy density, longer cycle life, and lower cost.^[1–3] Over the past two decades,

Z. Lun, Dr. B. Ouyang, Y. Tian, T. Shi, Prof. G. Ceder
Materials Science Division
LBNL
Berkeley, CA 94720, USA

Dr. B. Ouyang, Dr. D. A. Kitchaev, Dr. R. J. Clément,^[†]
Dr. M. Balasubramanian, Dr. J. Lee,^[††] Prof. B. D. McCloskey,
Prof. G. Ceder
Department of Materials Science and Engineering
UC Berkeley
Berkeley, CA 94720, USA
E-mail: jinhyuk@mit.edu; gceder@berkeley.edu

 The ORCID identification number(s) for the author(s) of this article can be found under <https://doi.org/10.1002/aenm.201802959>.

^[†]Present address: Materials Department, University of California, Santa Barbara, CA 93106, USA

^[††]Present address: Department of Nuclear Science and Engineering, MIT, Cambridge, MA 02139, USA

DOI: 10.1002/aenm.201802959

Dr. D. A. Kitchaev
Department of Materials Science and Engineering
MIT
Cambridge, MA 02139, USA
J. K. Papp, Prof. B. D. McCloskey
Department of Chemical and Biomolecular Engineering
UC Berkeley
Berkeley, CA 94720, USA
Dr. M. Balasubramanian
X-Ray Science Division
Advanced Photon Source
Argonne National Laboratory
Argonne, IL 60439, USA
T. Lei
Department of Chemistry
UC Berkeley
Berkeley, CA 94720, USA
Prof. B. D. McCloskey
Energy Storage and Distributed Resources Division
LBNL
Berkeley, CA 94720, USA

cation-disordered rock salt (DRX) structures because of the presence of locally lithium-rich environments, in which fluorine preferentially incorporates.^[19] This contrasts with the inability to fluorinate well-ordered layered cathode materials which always show formation of LiF instead.^[20] Fluorination has been shown to improve capacity retention and suppress irreversible oxygen loss, which are often observed when oxygen redox processes are active.^[21,22] But the underlying structural mechanism by which fluorination improves cyclability is not clear yet.

Fe and Mn are two of the more inexpensive and earth-abundant redox centers that can in principle be used in DRX materials. Fe–Nb- and Fe–Ti-based DRXs have been reported, but in general show lower discharge energy densities compared with Mn redox systems.^[9,18,23] Mn redox-based DRXs have shown very promising electrochemical performance but with some capacity fading. $\text{Li}_{1.3}\text{Mn}_{0.4}\text{Nb}_{0.3}\text{O}_2$ prepared using a traditional solid-state synthesis method exhibits a large initial capacity of $>290 \text{ mAh g}^{-1}$ (60°C , 10 mA g^{-1}) based partially on $\text{Mn}^{3+}/\text{Mn}^{4+}$ redox in addition to a large amount of oxygen redox, but suffers from substantial capacity fading upon extended cycling.^[9] Highly fluorinated $\text{Li}_{1.9}\text{Mn}_{0.95}\text{O}_{2.05}\text{F}_{0.95}$ obtained via a mechanochemical ball-milling synthesis delivers a capacity of 280 mAh g^{-1} , a larger fraction of which is supported by the $\text{Mn}^{3+}/\text{Mn}^{4+}$ redox capacity.^[24] The recently reported $\text{Li}_2\text{Mn}_{2/3}\text{Nb}_{1/3}\text{O}_2\text{F}$ / $\text{Li}_2\text{Mn}_{1/2}\text{Ti}_{1/2}\text{O}_2\text{F}$ ^[5] and $\text{Li}_{1.2}\text{Mn}_{0.2}\text{V}_{0.6}\text{O}_2$ ^[10] compounds prepared by mechanochemical synthesis rely mainly on $\text{Mn}^{2+}/\text{Mn}^{4+}$ redox (for $\text{Li}_{1.2}\text{Mn}_{0.2}\text{V}_{0.6}\text{O}_2$, $\text{V}^{4+}/\text{V}^{5+}$ redox as well) to achieve high capacities over 300 mAh g^{-1} (room temperature, 20 mA g^{-1}).

In this work, we combine $\text{Mn}^{3+}/\text{Mn}^{4+}$ redox and Nb^{5+} as a charge compensator with fluorination and investigate a class of Mn^{3+} – Nb^{5+} -based DRX oxyfluorides ($\text{Li}_{1.2}\text{Mn}^{3+}_{0.6+0.5x}\text{Nb}^{5+}_{0.2-0.5x}\text{O}_{2-x}\text{F}_x$, $x = 0, 0.05, 0.1, 0.15$, referred to as “LMNO,” “LMF05,” “LMF10,” and “LMF15,” respectively. A compound with $x = 0.2$, “LMF20,” was also synthesized as an example where the F solubility limit is exceeded). Like other d^0 -TM, Nb^{5+} promotes the formation and stabilization of the DRX structures by its ability to accommodate large octahedral distortions without substantial energy cost.^[25] By systematically varying the fluorine content, we show that capacity and cyclability can be improved by fluorination, but that a trade-off exists with higher fluorination, generally leading to more stable materials with less capacity loss even as total energy density decreases once an optimal F content is reached. Combining spectroscopic and computational tools, we reveal some possible origins of the improved capacity retention upon fluorination.

2. Results

2.1. Synthesis and Characterization

All the materials were prepared using a one-step solid-state synthesis, as described in the Experimental Section. The X-ray diffraction (XRD) patterns (Figure 1a) of LMNO, LMF05, LMF10, and LMF15 confirm the formation of disordered rock salt structures with no observable long-range ordering or

impurity peaks. The exact compositions of the compounds, determined using inductively coupled plasma optical emission spectrometry (ICP-OES), are listed in Table S1 (Supporting Information). With increased fluorine substitution, the lattice constant decreases from 4.2124 \AA (LMNO) to 4.1730 \AA (LMF05), 4.1710 \AA (LMF10), and 4.1694 \AA (LMF15). The particle size of the as-synthesized material is $\approx 300\text{--}400 \text{ nm}$, as observed in the transmission electron microscopy (TEM) image of LMF10 in Figure 1c. The scanning electron microscopy (SEM) images in Figure S2 (Supporting Information) further confirm the similar primary particle sizes of the four materials and reveal agglomeration of primary particles into secondary particles with $\approx 1 \mu\text{m}$ in size. Detailed refinement of the XRD patterns and SEM images of the four compounds are presented in Figures S1 and S2 (Supporting Information), respectively.

Although no sign of a LiF impurity phase was observed in the XRD patterns, we used ^{19}F solid-state nuclear magnetic resonance (ssNMR) spectroscopy as well as TEM–energy dispersive spectroscopy (EDS) mapping to further confirm that all the fluorine was incorporated in the material rather than forming a LiF impurity phase, as is the case for layered rock salts.^[20] ^{19}F NMR is particularly useful as it is highly sensitive in detecting small amount (down to 0.5%) of F in a diamagnetic environment (as in LiF) out of the large amount of F in the bulk paramagnetic environment. The ^{19}F NMR spectra for LMF05, LMF10, and LMF15, as well as for LiF powder and an empty rotor for reference, are presented in Figure 1b. As the signal at $\approx -163 \text{ ppm}$ originates from the probe, the very broad signals spanning the frequency range from -1000 to 500 ppm are assigned to F nuclei in the as-synthesized powders. As discussed in previous NMR studies on related oxyfluoride materials,^[5,10,26,27] these broad features arise from strong paramagnetic interactions between F nuclei and nearby transition metal species with unpaired d electrons (Mn^{3+} in this case). Paramagnetic interactions also lead to rapid relaxation of the ^{19}F NMR signal; therefore, the time delay between the excitation pulse and signal acquisition (i.e., the dwell time in the NMR experiment) should be as short as possible. A $0.1 \mu\text{s}$ delay was used for LMF05, which was shortened to $0.05 \mu\text{s}$ for LMF10 and LMF15, resulting in more intense ^{19}F paramagnetic signals in the spectra collected on the latter compounds. The absence of a sharp diamagnetic signal at -204 ppm indicates that no LiF impurity was present in LMF05, LMF10, or LMF15, and, hence, that all of the F has integrated in the bulk lattice. Furthermore, the TEM–EDS mapping of LMF10 in Figure 1d provides visual evidence of the successful F substitution and homogenous distribution of F atoms.

2.2. Electrochemical Performance

The cycling performance of the materials was tested in galvanostatic charge–discharge mode. Figure 2 presents voltage profiles of LMNO, LMF05, LMF10, and LMF15 between 1.5 and 4.8 V at 10 mA g^{-1} and room temperature. Without fluorination, LMNO delivers a discharge capacity (energy density) of 238 mAh g^{-1} (2870 Wh L^{-1} , 703 Wh kg^{-1}). With 2.5%, 5%, and 7.5% fluorine substitution, LMF05, LMF10, and LMF15 deliver higher

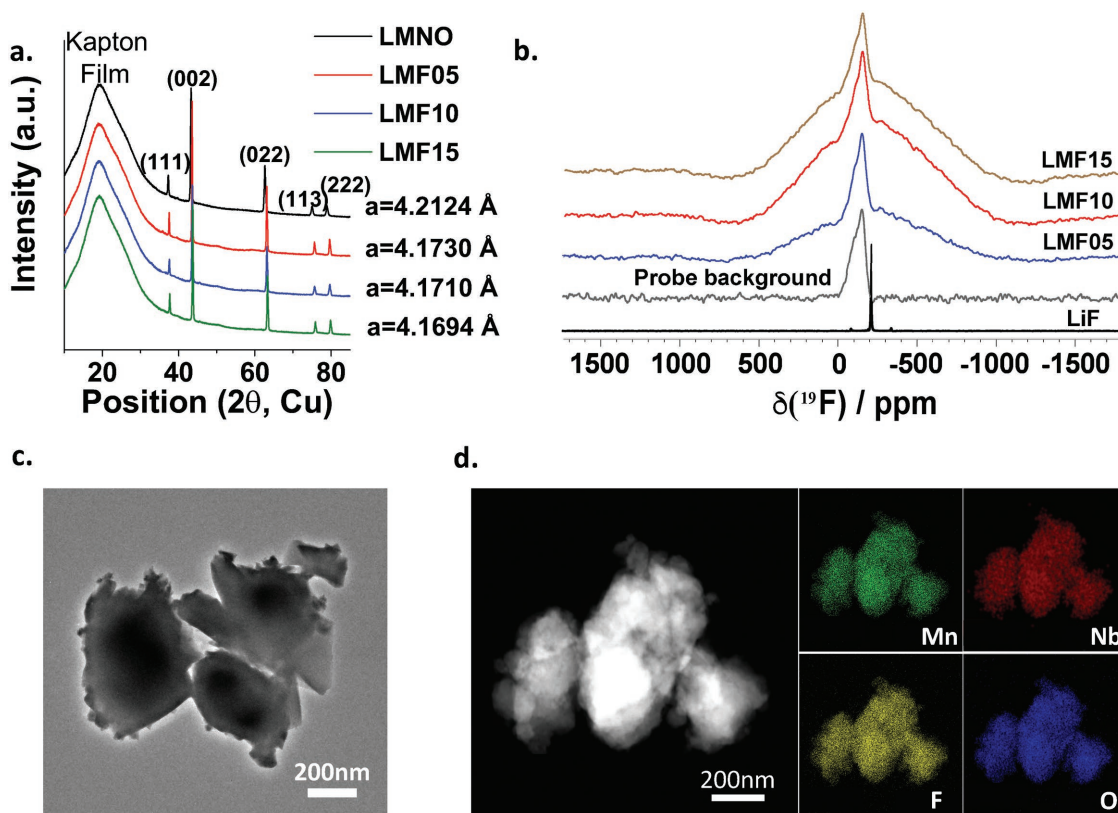


Figure 1. Structural characterization of Li-Mn-Nb-O(-F) compounds. a) XRD patterns and refined lattice constants of the as-synthesized LMNO, LMF05, LMF10, and LMF15. The very broad signals between 10° and 30° are the background signal from the Kapton film used to cover the samples. b) ^{19}F NMR sum spectra for the as-synthesized LMF05, LMF10, and LMF15 obtained by summing over four spin echo subspectra collected at different excitation frequencies. For comparison, ^{19}F spin echo spectra collected on LiF powder and an empty rotor (to isolate the probe background signal centered around -163 ppm) are overlaid. The sum spectra were scaled using the intensity of the probe background signal. c) TEM image of the as-synthesized LMF10 particles. d) TEM/EDS mapping of the elemental distribution in a representative particle cluster of the as-synthesized LMF10.

(or comparable for LMF15) initial discharge capacities (energy densities) than LMNO, reaching 272 mAh g^{-1} (3425 Wh L^{-1} , 823 Wh kg^{-1}), 252 mAh g^{-1} (3136 Wh L^{-1} , 759 Wh kg^{-1}), and 233 mAh g^{-1} (2911 Wh L^{-1} , 710 Wh kg^{-1}), respectively.

In addition to the higher capacities and energy densities, fluorination also greatly improves the capacity retention, as observed in the insets of the voltage profiles in Figure 2. After cycling between 1.5 and 4.8 V at 10 mA g^{-1} for 20 cycles, 84.3% and 92.4% of the initial capacities of LMF05 and LMF10 are retained, respectively, compared with only 80.7% for LMNO. LMF15 exhibits almost no capacity fade. The improvement of the capacity retention with increasing fluorination is more obvious at a higher cycling rate of 20 mA g^{-1} (as observed in Figure S4 in the Supporting Information): 62.7%, 77.9%, and 93.3% of the initial capacity is retained after 50 cycles for LMNO, LMF05, and LMF10, respectively.

2.3. Gas Evolution Measurement

Figure 3a–c presents the results of operando gas evolution measurements of LMNO, LMF05, and LMF10 during the first cycle, as obtained from differential electrochemical mass spectroscopy (DEMS) measurements. We measured the in

situ O_2 and CO_2 evolution while charging the cells from open-circuit voltage (OCV) to 4.8 V followed by discharge, all at a rate of 20 mA g^{-1} . As noted in previous work, most of the detected O_2 gas arises from oxygen near the surface of the cathode once it has undergone oxygen oxidation.^[22] The DEMS results suggest that fluorination substantially mitigates O loss: the O_2 gas evolution decreases from $0.066 \mu\text{mol mg}^{-1}$ for LMNO to $0.005 \mu\text{mol mg}^{-1}$ for LMF05, and for LMF10, only a negligible amount of O_2 gas can be observed. This finding indicates that the oxygen loss from LMNO is largely suppressed upon fluorination.

Reduced CO_2 gas evolution was also observed upon fluorination; however, the detected CO_2 likely originates from multiple degradation processes, as previously reported.^[28] Lee et al. prepared a $\text{Li}_2\text{Mn}_{1/2}\text{Ti}_{1/2}\text{O}_2\text{F}$ cathode using a similar sample preparation method and reported that at least 70% of the CO_2 gas evolved during cycling can be accounted for by decomposition of surface carbonate species (e.g., Li_2CO_3)^[5] with a low onset potential of $\approx 3.8\text{--}4 \text{ V}$.^[5,28] The carbonate forms either during mixing of the active materials with carbon or from unintended air exposure. The rest of the CO_2 gas released on charge presumably originates from either lattice oxygen at the surface or electrolyte decomposition, which usually occurs at high voltage $> 4.4 \text{ V}$.^[5,22,28] As indicated by the DEMS results,

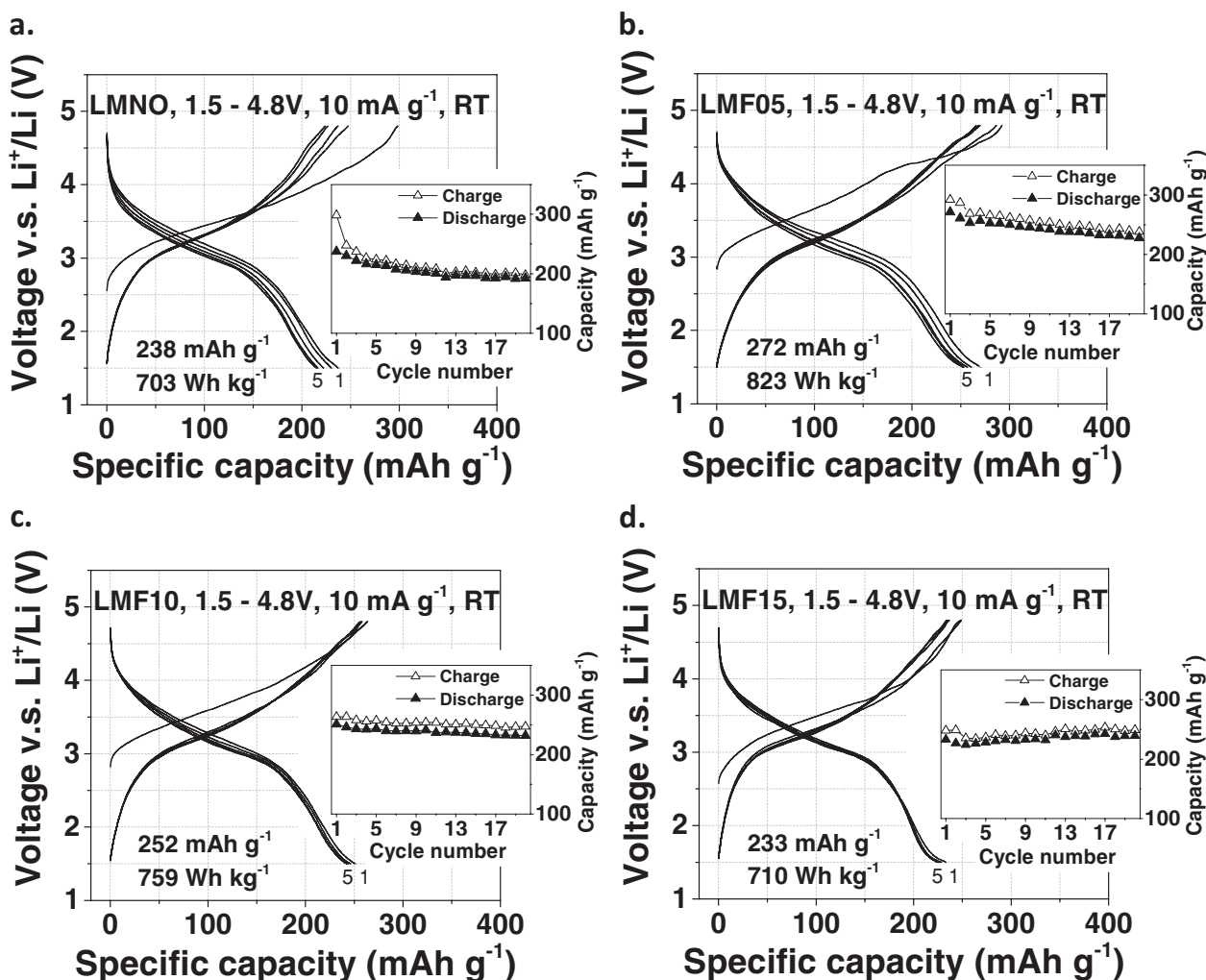


Figure 2. Electrochemical performance of a) LMNO, b) LMF05, c) LMF10, and d) LMF15. All the voltage profiles were collected within the voltage window of 1.5–4.8 V at 10 mA g⁻¹ at room temperature. The insets show the capacity retention of the materials over the first 20 cycles.

all three materials have similar onset voltages for CO₂ gas evolution near ≈3.8 V, resulting from the decomposition of the surface carbonate species. However, significantly more CO₂ was detected at high voltage for LMNO than for its fluorinated counterparts. Because all the cells were prepared using the same procedure and electrolyte, we may safely assume that the additional CO₂ gas released from LMNO is indicative of more severe oxygen loss from this material than from LMF05 and LMF10. Additionally, air-free X-ray photoelectron spectroscopy (XPS) spectra were collected to confirm that there is no significant difference in the content of surface carbonates or hydroxyl species, which can influence the amount of gas evolution during electrochemical cycling (Figure S5 and Table S2, Supporting Information).

2.4. Redox Mechanism

We combine X-ray absorption spectroscopy and ab initio calculations to understand the redox behavior of the materials. Figure 4a,c shows the Mn K-edge ex situ X-ray absorption

near-edge structure (XANES) of LMNO and LMF10 at five different states of charge in the initial cycle: pristine (“before”), charged to 3.6 V (“3.6 V c”), charged to 4.2 V (“4.2 V c”), charged to 4.8 V (“4.8 V c”), and charged to 4.8 V followed by discharge to 1.5 V (“1.5 V dc”). The XANES results indicate similar Mn redox behavior in LMNO and LMF10 during the charge process. The edge positions of both the pristine materials are close to that of Mn₂O₃, indicating that Mn is present as Mn³⁺. After charging the materials to 4.2 V (corresponding to the transfer of ≈0.7 mole of electrons per formula unit), the Mn K-edge shifts to a higher energy position close to that of MnO₂, indicating that Mn is oxidized from Mn³⁺ to Mn⁴⁺. Upon further charging to 4.8 V, the Mn K-edge barely shifts. After discharge, the Mn K-edge returns to its original position for LMF10; however, for LMNO, it is shifted to a lower energy than in the pristine sample. As the position and shape of the Mn K-edge spectra mostly depend on the oxidation state and local bonding environment of Mn,^[29] the larger change in the Mn K-edge spectrum of LMNO after a full cycle indicates more irreversible changes for LMNO than for LMF10. The irreversibility can originate either from the reduction of Mn to

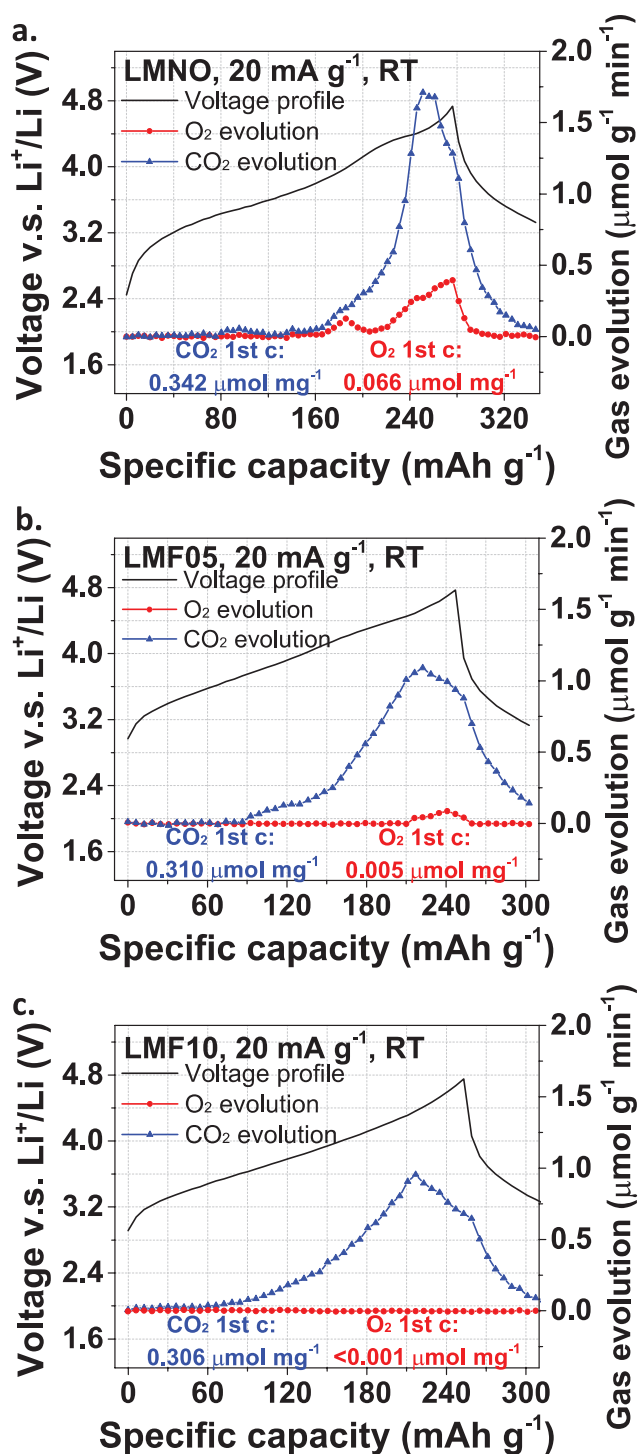


Figure 3. Operando DEMS results for a) LMNO, b) LMF05, and c) LMF10. The solid lines, red dots, and blue triangles correspond to the voltage profiles, O₂ evolution, and CO₂ evolution, respectively.

Mn²⁺ on discharge, which is often observed in cathode compounds that lose oxygen at high voltage,^[30,31] or from structural changes upon cycling. This finding is partially supported by the observation that more O₂ and CO₂ evolves from LMNO than from LMF10, in the DEMS measurements (Figure 3a,c). Nb⁵⁺

remains redox inactive during cycling, as can be seen from Figure S6 (Supporting Information).

Quantified analysis for XANES data is difficult at this stage, as there are no reported references for Mn-based disordered-oxyfluoride compounds. To obtain insight into the oxidation mechanism in these cathode materials, we used density functional theory (DFT) to calculate the voltage curves and Mn and O oxidation states upon delithiation (as shown in Figure 4b,d) for LMNO and LMF10. The calculations suggest that Mn redox accounts for most of the capacity below ≈ 4 V, whereas O redox dominates at high voltage. In addition, O oxidation occurs from lower potential in LMNO (above ≈ 0.5 Li extraction) than in LMF10 (above ≈ 0.6 Li extraction), and contributes more to the overall capacity for LMNO than for LMF10 (38.9% in LMNO vs 31.7% in LMF10 when 0.9 Li is extracted).

3. Discussion

3.1. Material Design and Electrochemical Performance

The main incentive for the substitution of O²⁻ by F⁻ is that it enables the use of more low-valent TMs, such as Ni²⁺, Mn²⁺, and Mn³⁺, which gives the cathode material a larger transition metal redox capacity. **Figure 5** presents a theoretical capacity map of the class of Mn³⁺-Nb⁵⁺-based compounds as a function of fluorination level (x in Li_{1.2}Mn³⁺_{0.6+0.5x}Nb⁵⁺_{0.2-0.5x}O_{2-x}F_x, $0 \leq x \leq 0.4$) for a fixed Li excess of 1.2 mole per formula unit. The blue triangles represent the theoretical capacity calculated assuming complete extraction of all Li⁺ ions from the material. The red stars represent the theoretical Mn³⁺/Mn⁴⁺ redox capacity. The Mn³⁺/Mn⁴⁺ theoretical capacity increases from 175 mAh g⁻¹ for Li_{1.2}Mn_{0.6}Nb_{0.2}O₂ to 251 mAh g⁻¹ for Li_{1.2}Mn_{0.8}O_{1.6}F_{0.4}. More importantly, the amount of anion redox required to achieve a large capacity, here taken as 250 mAh g⁻¹, is significantly reduced upon fluorination as can be seen from the green shaded area in Figure 5. For a compound with a multielectron redox-active TM, the increase of the theoretical TM capacity with fluorination is even more significant, as shown in Figure S7 (Supporting Information) for the example of Mn²⁺-Ti⁴⁺-based compounds. Our work also indicates that there is a limit to the amount of F that can be introduced in DRX compounds made through solid-state synthesis, which for Mn³⁺-Nb⁵⁺-based oxyfluorides fired at 1000 °C is estimated to be between 7.5% and 10% ($x = 0.15$ and 0.2), as marked by the black dashed line in Figure 5. This solubility limit is substantiated by the NMR results (Figure 1) which show that the LiF precursor is fully consumed in the synthesis of LMF05–LMF15. Although no LiF impurity phase is observed in the XRD pattern of LMF20 (Li_{1.2}Mn_{0.7}Nb_{0.1}O_{1.8}F_{0.2}) (Figure S8, Supporting Information), the ¹⁹F ssNMR spectrum in Figure S8b (Supporting Information) features a sharp signal at -204 ppm (with spinning sidebands marked with asterisks), suggesting the presence of LiF-like F environments in the sample, presumably because of the presence of a small amount of LiF phase. The more extended sideband pattern of LiF-like signals in the LMF20 spectrum, compared with that in the LiF spectrum, indicates long-range paramagnetic interactions between

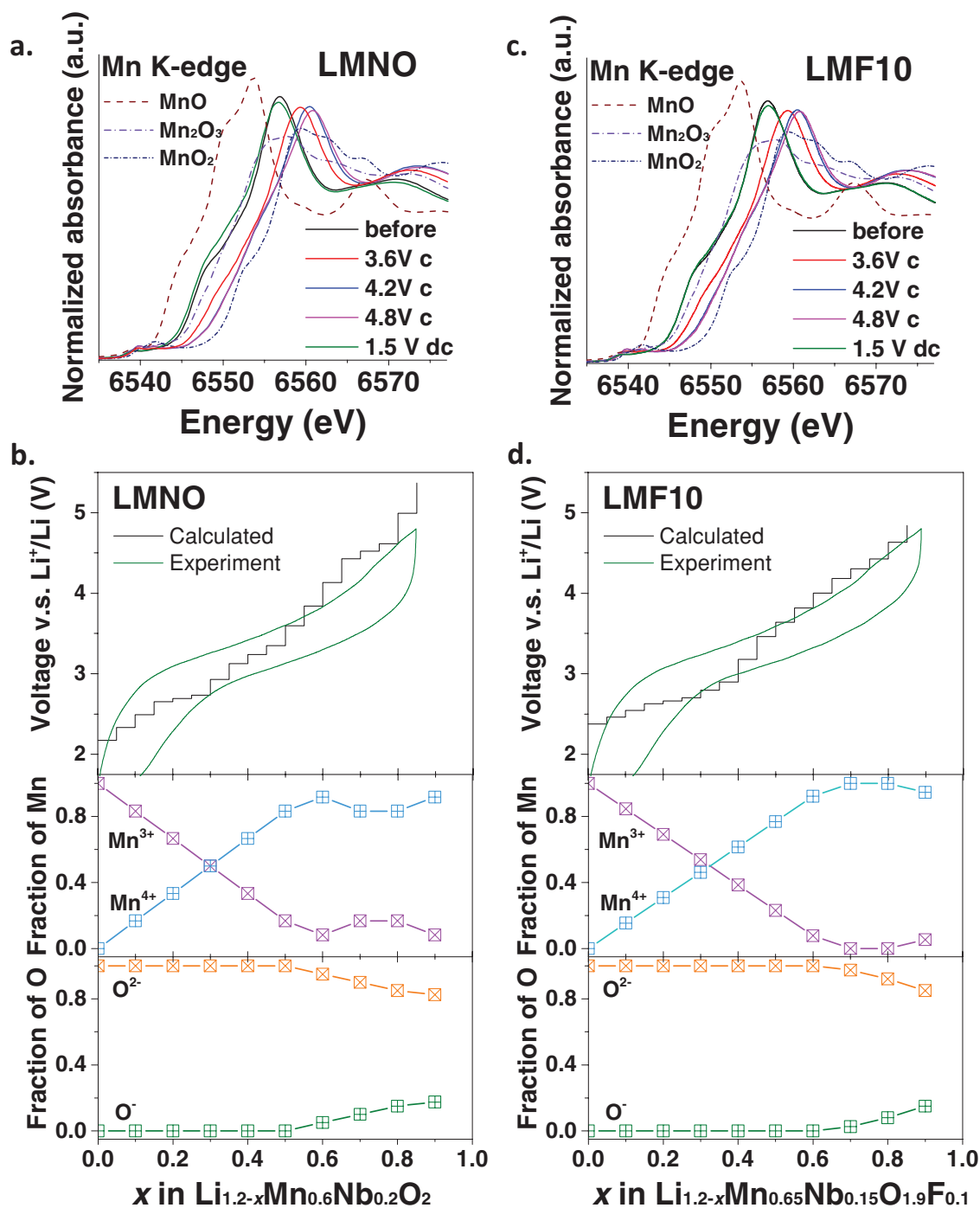


Figure 4. Redox mechanism in LMNO and LMF10 compounds. XANES of a) LMNO and c) LMF10 at Mn K-edge. Computed voltage profiles and evolution of Mn and O oxidation states calculated from DFT for b) LMNO and d) LMF10. The experimental voltage profiles are from the second cycle of each compound when cycling between 1.5 and 4.8 V at 10 mA g⁻¹.

F nuclei in LiF domains and Mn centers in the major LMF20 phase. We note that the longer dwell time used to acquire the ¹⁹F NMR spectrum for LMF20 (0.425 μs), compared with those used in the NMR experiments on LMF05, LMF10, and LMF15 (≤0.1 μs), likely accounts for the loss of the broad paramagnetic ¹⁹F NMR signals with short relaxation times in the LMF20 spectrum.

The optimal amount of fluorine substitution appears to be a trade-off between initial capacity and the capacity retention. **Figure 6** summarizes the electrochemical performance of LMNO, LMF05, and LMF10 at rates of 10 and 20 mA g⁻¹. The initial discharge capacity increases from 238 in LMNO to 272 mAh g⁻¹ in LMF05, but then drops with higher fluorination levels to 252 mAh g⁻¹ for LMF10 and 233 mAh g⁻¹ for LMF15.

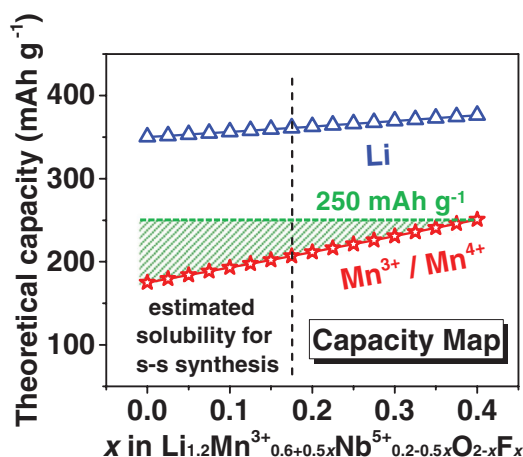


Figure 5. Theoretical capacity map of the class of $\text{Mn}^{3+}\text{--Nb}^{5+}$ compounds with fixed Li content (1.2 mole per formula unit) as a function of F content (x in $\text{Li}_{1.2}\text{Mn}^{3+}_{0.6+0.5x}\text{Nb}^{5+}_{0.2-0.5x}\text{O}_{2-x}\text{F}_x$, $0 \leq x \leq 0.4$). The blue triangles represent the theoretical capacity calculated assuming the full extraction of all the Li^+ ions. The red stars represent the theoretical $\text{Mn}^{3+}/\text{Mn}^{4+}$ redox capacity. The green shaded area represents the amount of anion redox required to achieve 250 mAh g^{-1} . The black dashed line represents the estimated solubility limit of LiF for solid-state synthesis at 1000°C .

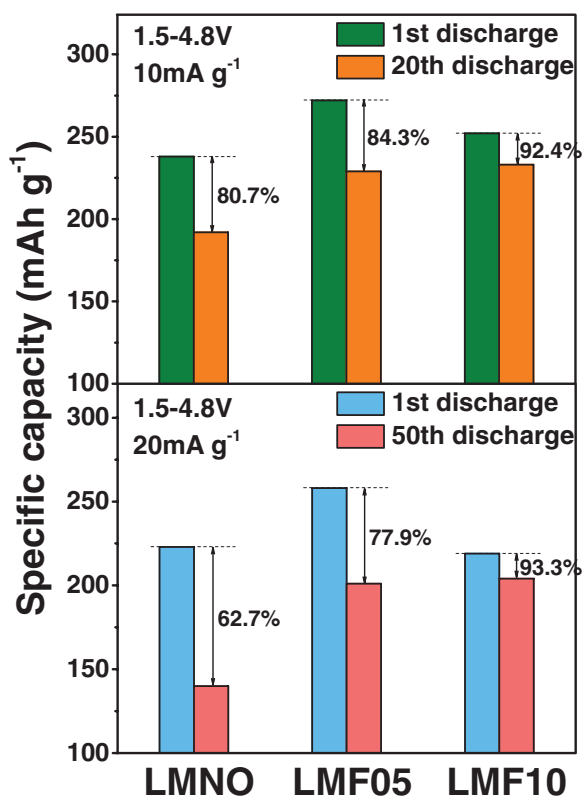


Figure 6. Comparison of discharge capacities of LMNO, LMF05, and LMF10. The top plot shows the 1st and 20th cycle discharge capacities for each compound when cycled between 1.5 and 4.8 V at a rate of 10 mA g^{-1} . The bottom plot shows the 1st and 50th cycle discharge capacities for each compound when cycled between 1.5 and 4.8 V at a rate of 20 mA g^{-1} . The numbers next to the bars represent the fraction of initial capacity retained after cycling.

Recent work^[10] has demonstrated that the strong Li–F bond limits the amount of Li that can be removed from the coordination shell of a F^- anion. For example, when a F atom is initially bonded with 6 Li within its first coordination shell, at most 5 Li ions can be extracted within a reasonable voltage window.

Despite this “Li-locking effect,” it is clear that fluorination can greatly improve the capacity retention, even though with less incorporation of d^0 stabilizer Nb^{5+} . With only 5% fluorine substitution, which corresponds to an increase of 8.3% in the Mn capacity, LMF10 achieves significantly better capacity retention than LMNO: LMNO and LMF10 retain 62.7% and 93.3% of their initial capacities, respectively, after 50 cycles between 1.5 and 4.8 V at a rate of 20 mA g^{-1} . This improvement is much more prominent than what was achieved by simply increasing the metal redox capacity in the Li–Ni–Ti–Mo system, where the 20-cycle capacity retention only improved from 79% to 82% in going from $\text{Li}_{1.2}\text{Ni}_{0.333}\text{Ti}_{0.333}\text{Mo}_{0.133}\text{O}_2$ to $\text{Li}_{1.15}\text{Ni}_{0.375}\text{Ti}_{0.375}\text{Mo}_{0.1}\text{O}_2$, which represents 12.6% more Ni redox.^[16] Apart from simply enabling more TM redox, we expect fluorination to produce some “bonus effect” to increase the structural stability of the materials.

3.2. Structural Origins of the Improved Capacity Retention upon Fluorination

To reveal the structural origin that may contribute to the improved capacity retention upon fluorination, we analyzed the bond length distribution of simulated LMNO and LMF10 structures. A cluster expansion approach^[10,19,32] was used to generate 20 snapshots of atomic arrangements (distributions of Li, Mn, Nb on the cation sites, and distributions of O and F on the anion sites of the rock salt structure, for both LMNO and LMF10). Each snapshot contains 80 atoms in a periodic unit cell and is generated using a canonical metropolis Monte Carlo sampling at the synthesis temperature (1000°C) followed by structural relaxation using the non-empirical strongly constrained and appropriately normed meta-GGA (SCAN) functional in DFT. In all 20 structures, the bond-length distribution around Mn, defined as the difference between the longest and shortest Mn–O/F bonds in an octahedron, is displayed in Figure 7a. Most of the octahedral Mn–O/F units in LMNO have a bond length deviation between 0.4 and 0.5 Å, with a maximum at ≈ 0.45 Å, consistent with the difference between short and long bonds around a Jahn–Teller (JT) active Mn^{3+} ion reported previously.^[33] In LMF10, bond length variation is lower by $\approx 33\%$, with most bond-length deviations lying between 0.25 and 0.35 Å with a maximum at ≈ 0.3 Å, indicating that fluorination helps to reduce the Mn^{3+} JT distortion. Though the effect of strain and volume change on capacity loss is generally poorly understood, it is possible that this reduction in local strain may contribute to the capacity retention.

To investigate changes in the JT distortion upon fluorination, we performed Mn extended X-ray absorption fine structure (EXAFS) analysis at different states of charge in the first cycle. The results are shown in Figure 7b. According to Yoon et al. and Terada et al., a lower intensity of the first peak in the TM EXAFS spectra, which represents the bonding information between TMs and their nearest anions, indicates

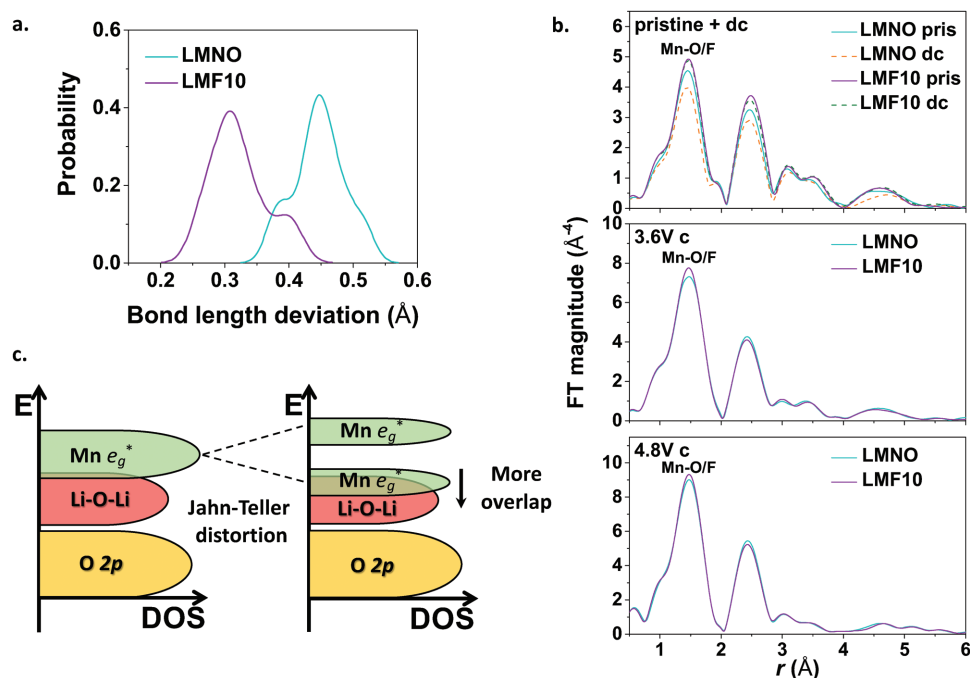


Figure 7. Structural origin of improved cyclability after fluorination. a) Distribution of calculated bond-length deviations in LMNO and LMF10 between Mn and their nearest neighbors. The bond-length deviation is defined as the difference between the longest Mn–O/F bond and the shortest Mn–O/F bond within the octahedral unit of a Mn atom and its six nearest neighbors (either F or O). b) Mn EXAFS spectra for LMNO and LMF10 at different states of charge in the first cycle: pristine and charged to 4.8 V followed by discharge to 1.5 V (upper), charged to 3.6 V (middle), and charged to 4.8 V (lower). c) Proposed structural connection between Jahn–Teller distortion and orbital energy levels.

more JT distortion in the material.^[30,34] Following this interpretation, the data in Figure 7b indicate that the pristine LMNO material has a larger JT distortion than LMF10 (upper panel). This interpretation of the EXAFS is consistent with the DFT results in Figure 7a. During charge, Mn^{3+} is gradually oxidized to Mn^{4+} , resulting in the intensity growth of the Mn–O/F EXAFS peak in both the materials, but LMNO retains more distortion than LMF10 even at the top charge. In the fully discharged samples shown in the upper panel of Figure 7b, the intensity of Mn–O/F peak further decreases compared with the pristine spectra for LMNO, indicating that LMNO becomes more distorted, while LMF10 shows pretty good reversibility, with no observable increase in the structural distortion.

We believe that the symmetry breaking of the electronic environment around Mn^{3+} by F is responsible for the reduction of the JT distortion in LMF10. For a regular Mn^{3+}O_6 octahedron (d^4 electronic configuration), the electronic symmetry of the ligands creates the degeneracy of the e_g orbitals, which is lifted by the spontaneous lengthening one of the octahedral axes, while reducing the other two. This symmetry breaking comprises the JT effect. The introduction of F around Mn breaks the electronic symmetry of the octahedron (even if the geometric symmetry remains), because of the different hybridization of F and O with Mn. Hence, even in a regular octahedron, the two e_g orbitals are no longer degenerate, and a JT distortion is less needed.

We further argue that specific to Mn^{3+} , a reduction in local distortion is likely to reduce the oxygen redox activity, as schematically illustrated in Figure 7c. A JT distortion splits the

degenerate Mn e_g^* orbitals, shifting one to lower and one to higher energy. This shift brings the filled lower JT orbital closer to the Li–O–Li states^[21] potentially creating overlap between these Mn and O states. Such overlap of Mn states associated with longer bonds was already noted by Lee et al.^[5] who suggested that it accounts for the inability to fully oxidize all Mn to Mn^{4+} in $\text{Li}_2\text{Mn}_{2/3}\text{Nb}_{1/3}\text{O}_2\text{F}$. Hence, besides the fact that fluorinated DRX materials have more Mn present, fluorination may also enhance the fraction of Mn that can be fully oxidized before oxygen oxidation sets in. These two features are likely to enhance the cycling stability of LMF10 over that of LMNO.

Since oxygen oxidation is most detrimental on the surface, where oxygen loss and resulting structural densification can occur,^[16] these improvements may be particularly effective at the surface where any oxygen loss would leave behind a TM-enriched layer.

4. Conclusion

In this work, we successfully incorporated fluorine in the disordered rock salt structure of $\text{Li}_{1.2}\text{Mn}_{0.6}\text{Nb}_{0.2}\text{O}_2$, increasing the energy density and significantly improving the capacity retention. Using a combination of spectroscopic and ab initio tools, we identified the significantly reduced oxygen loss during cycling, and the reduced JT distortion around Mn^{3+} as two possible causes of the improved cyclability with fluorination. We further propose that fluorination can alter the position of orbital energy levels and reduce the overlap between the Mn orbitals

and O orbitals near and below the Fermi level. This discovery provides us with a new strategy to stabilize the JT species and increase the structural stability and capacity retention for Li-ion cathode materials.

5. Experimental Section

Synthesis: All Li–Mn–Nb–O(–F) compounds were synthesized by a traditional solid-state method. Li_2CO_3 (Alfa Aesar, ACS, 99% min), MnO_2 (Alfa Aesar, 99.9%), Nb_2O_5 (Alfa Aesar, 99.9%), and LiF (Alfa Aesar, 99.99%) were used as precursors. All the precursors were stoichiometrically mixed (except for adding 5% more Li_2CO_3 in order to compensate possible loss during synthesis^[16,26]) with a Retsch PM 200 planetary ball mill at a rate of 300 rpm for 4 h. The precursors were then pelletized and sintered at 1000 °C under argon atmosphere for 7 h, followed by quenching at argon atmosphere. The pellets were then transferred to a glove box and ground into powders.

Electrochemistry: All cathode films were composed of active materials, SUPER C65 (Timcal), and polytetrafluoroethylene (PTFE, DuPont, Teflon 8A) at a weight ratio of 70:20:10. To make the cathode films, 280 mg active materials and 80 mg SUPER C65 were mixed and shaker-milled for 1 h in argon atmosphere with SPEX 800M Mixer/Mill, and PTFE was later added and manually mixed with the shaker-milled mixture for 40 min. The components were then rolled into thin films inside the glove box. Commercialized 1 M LiPF₆ in ethylene carbonate (EC) and dimethyl carbonate (DMC) solution (volume ratio 1:1) was used as electrolyte. Glass microfibers (Whatman) were used as separator. FMC Li metal foil was used as anode. Coin cells were assembled inside the glove box and tested on Arbin battery test instrument at room temperature. The loading density of the films was around 3 mg cm^{−2} based on active materials. The specific capacities were then calculated based on the weight of active materials (70%) in the cathode films.

Characterization: XRD patterns for the as-synthesized compounds were collected using a Rigaku MiniFlex diffractometer (Cu source) in a 2θ range of 5°–85° and Rietveld refinement was done with PANalytical X'pert HighScore Plus software. Elemental analysis was performed by Luvak Inc. with direct current plasma emission spectroscopy (ASTM E 1079-12) for lithium, manganese, niobium, and with an ion selective electrode (ASTM D 1179-10) for fluorine. SEM images were collected using a Zeiss Gemini Ultra-55 Analytical Field Emission SEM in the Molecular Foundry at Lawrence Berkeley National Lab (LBNL). Scanning transmission electron microscopy (STEM)/EDS measurements were performed on a JEM-2010F microscope equipped with an X-mas EDS detector in the Molecular Foundry at LBNL. Air-free XPS measurements were performed on a Thermo Scientific K-Alpha XPS System with a monochromatic Al Kα X-ray source in the Molecular Foundry at LBNL. The as-synthesized samples were mixed with carbon black (70:20) and shaker-milled for 1 h. The mixtures were then transferred into the XPS system using a Thermo Scientific KAlpha Vacuum Transfer Module to avoid air exposure. The spectra were acquired with passing energy of 50 eV and a dwell time of 50 ms. Data analysis was performed using Thermo Fisher Advantage software.

Solid-State Nuclear Magnetic Resonance (NMR) Spectroscopy: ¹⁹F NMR data were obtained at room temperature using a Bruker Avance 500 MHz (11.7 T) wide-bore NMR spectrometer, at a Larmor frequency of −470.7 MHz. The spectra were acquired under 60 kHz magic angle spinning (MAS), using a 1.3 mm double-resonance probe, and chemical shifts were referenced against lithium fluoride powder (LiF, δ_{iso}(¹⁹F) = −204 ppm).

Because the resonant frequency range of the ¹⁹F nuclei in the as-synthesized LMF05, LMF10, and LMF15 cathodes was larger than the excitation bandwidth of the radio frequency (RF) pulse used in the NMR experiment, four spin echo spectra were collected for each sample, with the irradiation frequency varied in steps of 250 ppm or 118 kHz from −740 to 10 ppm. The individual subspectra were processed using a zero order phase correction so that the on-resonance signal was in

the absorption mode. The four subspectra were then added to give an overall sum spectrum with no further phase correction required. This “frequency stepping,”^[35] “spin echo mapping,”^[36] or “VOCS”^[37] (variable offset cumulative spectrum) methodology provides a large excitation bandwidth with uniform excitation of the broad ¹⁹F signals. For LMF05, a dwell time of 0.1 μs was used, while for LMF10 and LMF15, a shorter dwell time of 0.05 μs was employed to reduce signal relaxation prior to signal acquisition. Individual ¹⁹F spin echo spectra were collected using a 90° RF excitation pulse of 1.6 μs and a 180° RF pulse of 3.2 μs at 76.3 W (or 156 kHz), with a recycle delay of 50 ms. For comparison, a spin echo spectrum was collected on LiF using similar RF pulses as for the LMF samples but a longer recycle delay of 60 s. A ¹⁹F probe background spin echo spectrum, acquired under similar conditions as the individual LMF spin echo spectra but on an empty rotor, revealed the presence of a background signal.

Ex Situ Hard X-Ray Absorption Spectroscopy (XAS): The XAS of Mn K-edge was acquired in transmission mode at beamline 20-BM-B in Advanced Photon Source. The incident beam energy was selected using a Si (111) monochromator. The energy calibration was performed by simultaneously measuring the spectra of appropriate metal foil. Harmonic rejection was accomplished using a Rh-coated mirror. All the ex situ samples were electrodes films, composed of active materials, SUPER C65, and PTFE with weight ratio of 70:20:10, and loading density of 5 mg cm^{−2} (based on active materials). They were assembled as coin cells, charged to designated capacities, then disassembled and washed with DMC in glove box (except for pristine materials). Additional spectra of reference standards were also measured to facilitate the interpretation. The raw data were normalized and calibrated using Athena software.

Differential Electrochemical Mass Spectrometer (DEMS) Measurement: The custom-built DEMS and the cell geometry used were described in previous publications.^[38] The electrochemical cells used with the DEMS device were prepared in glove box using modified Swagelok design and the cathode film was composed of active materials, carbon black, and PTFE with weight ratio of 70:20:10, and loading density of ≈10 mg cm^{−2} (based on active materials). The assembled cells were charged at 20 mA g^{−1} under a static head of positive argon pressure (around 1.2 bar) after being appropriately attached to the DEMS. Throughout the charge, argon gas pulses periodically swept accumulated gases to a mass spectrometer chamber. The mass spectrometer absolute sensitivity was calibrated for CO₂ and O₂, and therefore the partial pressures of these gases could be determined. The amount of CO₂ and O₂ evolved was then quantified based on the volume of gas swept to the mass spectrometer per pulse.

Computational Methods: To evaluate the energetics, redox mechanism and atomic ordering of Li⁺–Mn³⁺–Nb⁵⁺–O^{2−}, a combination of DFT calculations, together with cluster expansion and Monte Carlo simulations used in the previous reports were applied.^[10,19] Within the LiF–LiMnO₂–LiNbO₃ system, the cluster expansion consisting of pair interactions up to 7.1 Å, triplet interactions up to 4.0 Å, and quadruplet interactions up to 4.0 Å based on a primitive rock salt lattice was constructed using DFT-calculated energies. The effective cluster interactions and dielectric constant were obtained from a L1-regularized least square regression,^[39] with the regularization parameters chosen to minimize cross-validation error.^[39] By this procedure, a root-mean-squared error below 7 meV atom^{−1} was obtained.

The DFT calculations were performed with the Vienna ab initio simulation package (VASP)^[40] and the projector-augmented wave (PAW) method.^[41] For each of the structural optimization calculation, a reciprocal space discretization of 25 Å was applied, and the convergence criteria were set as 10^{−6} eV for electronic loops and 0.02 eV Å^{−1} for ionic loops. The Perdew–Burke–Ernzerhof functional exchange–correlation functional with the rotationally averaged Hubbard *U* correction^[42] was applied for obtaining more accurate DFT energetics, the *U* parameters were chosen from a previously reported calibration to oxide formation energies^[43] (1.5 eV for Nb and 3.9 eV for Mn).

In order to understand the atomic ordering of the disordered rock salt system with Mn³⁺/Nb⁵⁺ cations, canonical Monte Carlo sampling of full lithiated structure using the Metropolis–Hastings algorithm^[44]

was performed on different compositions and temperatures on base of the cluster expansion parameterization. For atomic ordering analysis, 500 different $8 \times 8 \times 10$ super cells consisting of 1280 atoms each were sampled with Monte Carlo for good statistics.

To study the delithiation behavior, all possible Li-vacancy ordering in small supercells were enumerated with energies calculated by SCAN meta-GGA exchange–correlation functional^[45] due to its reliable ranking of structure energetics.^[46] With energetics evaluated by SCAN, the delithiated cluster expansion was then fitted as an offset from a baseline of formal charge electrostatics. The various oxidation states of Mn and O were treated as different species and were identified according to their magnetic moment from SCAN calculations. The final root-mean-square error of this cluster expansion was less than 5 meV atom⁻¹. With the established delithiated cluster expansion, the most stable Li-vacancy ordering at each delithiation stage was fully relaxed for constructing the voltage curve. The pymatgen code was utilized for all the structure analysis and postprocessing.

Supporting Information

Supporting Information is available from the Wiley Online Library or from the author.

Acknowledgements

This work was supported by the Umicore Specialty Oxides and Chemicals, and the Assistant Secretary for Energy Efficiency and Renewable Energy, Vehicle Technologies Office, of the U.S. Department of Energy under Contract No. DEAC02-05CH11231, under the Advanced Battery Materials Research (BMR) Program. Work at the Molecular Foundry was supported by the Office of Science, Office of Basic Energy Sciences, of the U.S. Department of Energy under Contract No. DE-AC02-05CH11231. The authors would like to acknowledge Dr. Jerry Hu and the California NanoSystems Institute (CNSI) at the University of California Santa Barbara (UCSB) for experimental time on the 500 MHz NMR spectrometer. The NMR experimental work reported here made use of the shared facilities of the UCSB MRSEC (Grant No. NSF DMR 1720256), a member of the Material Research Facilities Network. This research used resources of the Advanced Photon Source, an Office of Science User Facility operated for the U.S. Department of Energy (DOE) Office of Science by Argonne National Laboratory, and was supported by the U.S. DOE under Contract No. DE-AC02-06CH11357. The authors thank Jingyang Wang for help of the XAS measurement. The computational analysis was performed using computational resources sponsored by the Department of Energy's Office of Energy Efficiency and Renewable Energy and located at the National Renewable Energy Laboratory, computational resources provided by Extreme Science and Engineering Discovery Environment (XSEDE), which was supported by the National Science Foundation Grant Number ACI1053575, as well as the National Energy Research Scientific Computing Center (NERSC), a DOE Office of Science User Facility supported by the Office of Science and the U.S. Department of Energy under Contract No. DE-AC02-05CH11231. The authors thank Dr. Huiwen Ji, Dr. Deok-Hwang Kwon, and Dr. Hyunchul Kim for helpful discussion.

Z.L. planned the project with J.L. and G.C.; Z.L. designed, synthesized, characterized (XRD), and electrochemically tested the proposed compounds with the help from J.L.; B.O. and D.A.K. performed DFT calculations and analyzed the data; R.J.C. acquired and analyzed the NMR data; J.K.P. acquired and analyzed DEMS data with input from B.D.M.; Z.L. acquired and analyzed the XAS data with the help from M.B.; Y.T. acquired and analyzed the XPS data; T.L. acquired and analyzed the TEM data; T.S. performed SEM. The paper was written by Z.L. and was revised by B.O., R.J.C., and G.C. with the help of other authors. All authors contributed to discussions.

Conflict of Interest

The authors declare no conflict of interest.

Keywords

cyclability, DFT, fluorination, Jahn–Teller distortion, Li-excess cation-disordered cathodes

Received: September 23, 2018

Revised: October 26, 2018

Published online: November 16, 2018

- [1] E. A. Olivetti, G. Ceder, G. G. Gaustad, X. Fu, *Joule* **2017**, 1, 229.
- [2] a) V. Etacheri, R. Marom, R. Elazari, G. Salitra, D. Aurbach, *Energy Environ. Sci.* **2011**, 4, 3243; b) J. B. Goodenough, K.-S. Park, *J. Am. Chem. Soc.* **2013**, 135, 1167.
- [3] K. Turcheniuk, D. Bondarev, V. Singhal, G. Yushin, *Nature* **2018**, 559, 467.
- [4] a) K. Kang, Y. S. Meng, J. Bréger, C. P. Grey, G. Ceder, *Science* **2006**, 311, 977; b) Z. Lu, D. MacNeil, J. Dahn, *Electrochem. Solid-State Lett.* **2001**, 4, A200; c) P. Rozier, J. M. Tarascon, *J. Electrochem. Soc.* **2015**, 162, A2490.
- [5] J. Lee, D. A. Kitchaev, D.-H. Kwon, C.-W. Lee, J. K. Papp, Y.-S. Liu, Z. Lun, R. J. Clément, T. Shi, B. D. McCloskey, J. Guo, M. Balasubramanian, G. Ceder, *Nature* **2018**, 556, 185.
- [6] J. Lee, A. Urban, X. Li, D. Su, G. Hautier, G. Ceder, *Science* **2014**, 343, 519.
- [7] A. Urban, J. Lee, G. Ceder, *Adv. Energy Mater.* **2014**, 4, 1400478.
- [8] R. Wang, X. Li, L. Liu, J. Lee, D.-H. Seo, S.-H. Bo, A. Urban, G. Ceder, *Electrochem. Commun.* **2015**, 60, 70.
- [9] N. Yabuuchi, M. Takeuchi, M. Nakayama, H. Shiiba, M. Ogawa, K. Nakayama, T. Ohta, D. Endo, T. Ozaki, T. Inamasu, K. Sato, S. Komaba, *Proc. Natl. Acad. Sci. USA* **2015**, 112, 7650.
- [10] D. A. Kitchaev, Z. Lun, W. D. Richards, H. Ji, R. J. Clément, M. Balasubramanian, D.-H. Kwon, K. Dai, J. K. Papp, T. Lei, B. D. McCloskey, W. Yang, J. Lee, G. Ceder, *Energy Environ. Sci.* **2018**, 11, 2159.
- [11] R. Chen, S. Ren, X. Mu, E. Maawad, S. Zander, R. Hempelmann, H. Hahn, *ChemElectroChem* **2016**, 3, 892.
- [12] S. Hoshino, A. M. Glushenkov, S. Ichikawa, T. Ozaki, T. Inamasu, N. Yabuuchi, *ACS Energy Lett.* **2017**, 2, 733.
- [13] R. Chen, S. Ren, M. Knapp, D. Wang, R. Witter, M. Fichtner, H. Hahn, *Adv. Energy Mater.* **2015**, 5, 1401814.
- [14] N. Twu, X. Li, A. Urban, M. Balasubramanian, J. Lee, L. Liu, G. Ceder, *Nano Lett.* **2015**, 15, 596.
- [15] T. Matsuhara, Y. Tsuchiya, K. Yamanaka, K. Mitsuhara, T. Ohta, N. Yabuuchi, *Electrochemistry* **2016**, 84, 797.
- [16] J. Lee, D.-H. Seo, M. Balasubramanian, N. Twu, X. Li, G. Ceder, *Energy Environ. Sci.* **2015**, 8, 3255.
- [17] A. Kitajou, K. Tanaka, H. Miki, H. Koga, T. Okajima, S. Okada, *Electrochemistry* **2016**, 84, 597.
- [18] S. L. Glazier, J. Li, J. Zhou, T. Bond, J. Dahn, *Chem. Mater.* **2015**, 27, 7751.
- [19] W. D. Richards, S. T. Dacek, D. A. Kitchaev, G. Ceder, *Adv. Energy Mater.* **2018**, 8, 1701533.
- [20] a) M. Ménétrier, J. Bains, L. Croguennec, A. Flambard, E. Bekaert, C. Jordy, P. Biensan, C. Delmas, *J. Solid State Chem.* **2008**, 181, 3303; b) L. Croguennec, J. Bains, M. Ménétrier, A. Flambard, E. Bekaert, C. Jordy, P. Biensan, C. Delmas, *J. Electrochem. Soc.* **2009**, 156, A349.

- [21] D.-H. Seo, J. Lee, A. Urban, R. Malik, S. Kang, G. Ceder, *Nat. Chem.* **2016**, 8, 692.
- [22] K. Luo, M. R. Roberts, R. Hao, N. Guerrini, D. M. Pickup, Y.-S. Liu, K. Edström, J. Guo, A. V. Chadwick, L. C. Duda, P. G. Bruce, *Nat. Chem.* **2016**, 8, 684.
- [23] N. Yabuuchi, M. Nakayama, M. Takeuchi, S. Komaba, Y. Hashimoto, T. Mukai, H. Shiiba, K. Sato, Y. Kobayashi, A. Nakao, *Nat. Commun.* **2016**, 7, 13814.
- [24] R. A. House, L. Jin, U. Maitra, K. Tsuruta, J. W. Somerville, D. P. Förstermann, F. Massel, L. Duda, M. R. Roberts, P. G. Bruce, *Energy Environ. Sci.* **2018**, 11, 926.
- [25] A. Urban, A. Abdellahi, S. Dacek, N. Artrith, G. Ceder, *Phys. Rev. Lett.* **2017**, 119, 176402.
- [26] J. Lee, J. K. Papp, R. J. Clément, S. Sallis, D.-H. Kwon, T. Shi, W. Yang, B. D. McCloskey, G. Ceder, *Nat. Commun.* **2017**, 8, 981.
- [27] R. J. Clément, D. Kitchaev, J. Lee, C. Gerbrand, *Chem. Mater.* **2018**, 30, 6945.
- [28] S. E. Renfrew, B. D. McCloskey, *J. Am. Chem. Soc.* **2017**, 139, 17853.
- [29] F. Farges, *Phys. Rev. B* **2005**, 71, 155109.
- [30] W.-S. Yoon, C. P. Grey, M. Balasubramanian, X.-Q. Yang, J. McBreen, *Chem. Mater.* **2003**, 15, 3161.
- [31] a) H. Koga, L. Croguennec, M. Ménétrier, P. Mannesiez, F. Weill, C. Delmas, S. Belin, *J. Phys. Chem. C* **2014**, 118, 5700; b) D. Buchholz, J. Li, S. Passerini, G. Aquilanti, D. Wang, M. Giorgetti, *ChemElectroChem* **2015**, 2, 85.
- [32] W. D. Richards, Y. Wang, L. J. Miara, J. C. Kim, G. Ceder, *Energy Environ. Sci.* **2016**, 9, 3272;
- [33] C. Marianetti, D. Morgan, G. Ceder, *Phys. Rev. B* **2001**, 63, 224304.
- [34] Y. Terada, K. Yasaka, F. Nishikawa, T. Konishi, M. Yoshio, I. Nakai, *J. Solid State Chem.* **2001**, 156, 286.
- [35] a) L. A. O'Dell, A. J. Rossini, R. W. Schurko, *Chem. Phys. Lett.* **2009**, 468, 330; b) A. J. Pell, R. J. Clément, C. P. Grey, L. Emsley, G. Pintacuda, *J. Chem. Phys.* **2013**, 138, 114201.
- [36] M. Sananes, A. Tuel, G. Hutchings, J. Volta, *J. Catal.* **1994**, 148, 395.
- [37] D. Massiot, I. Farnan, N. Gautier, D. Trumeau, A. Trokiner, J. P. Coutures, *Solid State Nucl. Magn. Reson.* **1995**, 4, 241.
- [38] a) B. D. McCloskey, D. Bethune, R. Shelby, G. Girishkumar, A. Luntz, *J. Phys. Chem. Lett.* **2011**, 2, 1161; b) B. D. McCloskey, R. Scheffler, A. Speidel, D. S. Bethune, R. M. Shelby, A. Luntz, *J. Am. Chem. Soc.* **2011**, 133, 18038; c) B. D. McCloskey, A. Speidel, R. Scheffler, D. Miller, V. Viswanathan, J. Hummelshøj, J. Nørskov, A. Luntz, *J. Phys. Chem. Lett.* **2012**, 3, 997.
- [39] L. J. Nelson, G. L. W. Hart, F. Zhou, V. Ozoliņš, *Phys. Rev. B* **2013**, 87, 035125.
- [40] G. Kresse, J. Furthmüller, *Comput. Mater. Sci.* **1996**, 6, 15.
- [41] G. Kresse, D. Joubert, *Phys. Rev. B* **1999**, 59, 1758.
- [42] S. L. Dudarev, G. A. Botton, S. Y. Savrasov, C. J. Humphreys, A. P. Sutton, *Phys. Rev. B* **1998**, 57, 1505.
- [43] L. Wang, T. Maxisch, G. Ceder, *Phys. Rev. B* **2006**, 73, 195107.
- [44] a) N. Metropolis, A. W. Rosenbluth, M. N. Rosenbluth, A. H. Teller, E. Teller, *J. Chem. Phys.* **1953**, 21, 1087; b) W. K. Hastings, *Biometrika* **1970**, 57, 97.
- [45] J. Sun, A. Ruzsinszky, J. P. Perdew, *Phys. Rev. Lett.* **2015**, 115, 036402.
- [46] a) D. A. Kitchaev, H. Peng, Y. Liu, J. Sun, J. P. Perdew, G. Ceder, *Phys. Rev. B* **2016**, 93, 045132; b) Y. Zhang, D. A. Kitchaev, J. Yang, T. Chen, S. T. Dacek, R. A. Sarmiento-Pérez, M. A. L. Marques, H. Peng, G. Ceder, J. P. Perdew, J. Sun, *npj Comput. Mater.* **2018**, 4, 9.